Electronic Supplementary Material (ESI) for CrystEngComm.

Supporting Information

An Adenosine Triphosphate-Responsive Mesoporous Metal-Organic Framework Decorated with Palladium Nanosheets for Synergistic tri-modal therapy

Lijia Yao, Wenqian Cao, Yuanjing Cui and Guodong Qian**

State Key Laboratory of Silicon Materials, Cyrus Tang Center for Sensor Materials and Applications, School of Materials Science and Engineering, Zhejiang University, Hangzhou 310027, China. E-mail: cuiyj@zju.edu.cn, gdqian@zju.edu.cn

1.Experimental section

1.1 Chemicals and Materials

Palladium(II) acetylacetonate ($Pd(acac)_2$, 99%)， polyvinyl pyrrolidone (PVP, MW = 29000), Oxalic acid (OA, 98%) and tungsten hexacarbonyl ($W(CO)_6$, 97%) were purchased from Sigma-Aldrich. Hexadecyltrimethylammonium bromide (CTAB), N, N-dimethylformamide (DMF, AR), ethanol (AR), and acetone (AR) were purchased from Sinopharm Chemical Reagent Co., Ltd.

All the chemicals and materials were used as received.

1.2 Apparatus

The size, morphology and microstructure of the samples was characterized by field emission scanning electron microscope (SEM, Hitachi S-4800) and transmission electron microscopy (TEM, HT-7700). Powder X-ray diffraction (XRD) patterns were obtained on a Shimadzu XRD7000 powder X-ray diffractometer with the recording rate $2^{o}\cdot min^{-1}$ in the 2θ = 3-20 degree at room temperature. UV-Vis absorbance spectroscopy was obtained on UV-2600 UV-Vis spectrophotometer (Shimadzu, Japan). Zeta potential were carried out on a Zetasizer Nano-ZS instrument (Malvern, England). The concentration of ions was measured by Inductive Coupled Plasma Emission Spectrometer (ICP, Varian-730ES). X-ray photoelectron spectroscopy (XPS) spectra were performed by ESCALAB 250XI system. Thermogravimetric analysis (TGA) was carried out on TG209F3 Thermal gravimetric Analyzer (NETZSCH, German). Fourier transform infrared (FTIR) spectra were collected on a Spectrum One in the spectral range of 400-4000 cm^{-1} (Thermo Scientific Nicolet iS20). N_2 sorption isotherms were

measured by Micromeritics ASAP 2460 surface area analyzer. N_2 sorption measurement was maintained at 77 K with liquid nitrogen. The CLSM study was performed on Olympus FV-1000 confocal laser scanning microscope.

1.3 Photothermal effect of MIL@Pd NPs

For measuring the photothermal conversion performance of MIL@Pd NPs, 2.0 mL of MIL@Pd NPs (0-200 μg mL^{-1}) were introduced in a quartz cuvette and irradiated with an 808 nm NIR laser at a power density of 2 W cm^{-2} for 600 s, respectively. The temperature was recorded every 10 s by a forward-looking infrared (FLIR) imaging instrument.

The photothermal conversion efficiency of MIL@Pd NPs was determined according to previous method. Detailed calculation was given as following:

Based on the total energy balance for this system:

$$\sum_i m_i C_{p,i} \frac{dT}{dt} = Q_{NPs} + Q_s - Q_{loss} \quad (1)$$

where m and C_p are the mass and the heat capacity of solvent (water), respectively. T is the solution temperature.

Q_{NPs} is the photothermal energy input by MIL@Pd NPs:

$$Q_{NPs} = I(1 - 10^{-A_\lambda})\eta \quad (2)$$

where *I* is the laser power, A_λ is the absorbance of MIL@Pd NPs at the wavelength of 808 nm, and the η is the conversion efficiency from the absorbed light energy to thermal energy.

Q_s is the heat associated with the light absorbance of the solvent, which is measured independently to be 25.2 mW using purie water without MIL@Pd NPs.

Q_{loss} is thermal energy lost to the surroundings:

$$Q_{loss} = hA\Delta\mathrm{T} \tag{3}$$

where h is the heat transfer coefficient, A is the surface area of the container, and $\Delta\mathrm{T}$ is the temperature change, which is defined as T-T_{surr} (T and T_{surr} are the solution temperature and ambient temperature of the surroundings, respectively).

At the maximum steady-state temperature, the heat input is equal to the heat output, that is:

$$Q_{NPs} + Q_s = Q_{loss} = hA\Delta T_{max} \tag{4}$$

where ΔT_{max} is the temperature change at the maximum steady-state temperature. According to the Eq.2 and Eq.4, the photothermal conversion efficiency (η) can be determined:

$$\eta = \frac{hA\Delta T_{max} - Q_S}{I(1 - 10^{-A_\lambda})} \tag{5}$$

In this equation, only hA is unknown for calculation. In order to get the hA, we herein introduce θ, which is defined as the radio of ΔT to ΔT_{max}:

$$\theta = \frac{\Delta T}{\Delta T_{max}} \tag{6}$$

Substituting Eq.6 into Eq.1 and rearranging Eq.1:

$$\frac{d\theta}{dt} = \frac{hA}{\sum_i m_i C_{p,i}}\left[\frac{Q_{NPs} + Q_s}{hA\Delta T_{max}} - \theta\right] \tag{7}$$

When the laser was shut off, the $Q_{NPs} + Q_s = 0$, Eq.7 changed to:

$$dt = -\frac{\sum_i m_i C_{p,i}}{hA}\frac{d\theta}{\theta} \tag{8}$$

Integrating Eq.8 gives the expression:

$$t = -\frac{\sum_i m_i C_{p,i}}{hA} ln\theta \quad (9)$$

Thus, *hA* can be determined by applying the linear time data from the cooling period vs –lnθ，Substituting *hA* value into Eq.5, the photothermal conversion efficiency (η) of MIL@Pd NPs can be calculated.

where τ is the slope of the linear time data from the coling period vs –lnθ (Fig. S11). m and Cp are the mass and heat capacity of water, respectively.

1.4 DOX loading and DOX-releasing experiment

The DOX loading capacity (LC) and loading efficiency (LE) were calculated according to the following equations.

$$\text{LC (\%)} = \frac{M_s - M_o}{M_m} \times 100\% \quad (1)$$

$$\text{LE (\%)} = \frac{M_s - M_o}{M_o} \times 100\% \quad (2)$$

where M_S is mass of DOX in the supernatant, M_O is mass of original DOX, M_m is mass of the MIL@Pd nanocomposites.

1.5 Cell culture

HeLa cells were cultured in high-glucose DMEM containing 10% inactivated fetal bovine serum (FBS) and 1% (penicillin and streptomycin) under humidified atmosphere with 5% CO_2 at 37 ^oC.

HL-7702 (L02, human normal liver cells) were cultured in RPMI 1640 containing

10% inactivated fetal bovine serum (FBS) and 1% (penicillin and streptomycin) under the same condition.

1.6 Intracellular ROS generation

To investigate the Fenton reaction, methylene (MB) and 3,5,3',5'-tetramethyl-benzidine (TMB) were used as indicator. The color of TMB will turn blue when oxidized by •OH. 20 μL of MB solution (10 mg/mL), 2 mL HEPES buffer, 200 μL MIL@Pd (1 mg/mL), and 100 μL H_2O_2 (8 mM) were added into cuvette. The production of •OH was monitored by the absorption at 663 nm at different time interval.

As for TMB, the manipulation is similar to that of MB. The production of •OH was monitored by the absorption at 652 nm at different time interval.

And the •OH production is also detected in solution at different pH (pH 7.4, pH 5.5).

2. Supporting Tables and Figures.

Table S1. Summary of Pd NSs-based nanocomposites for synergistic tumor therapy.

Synergistic Therapy	Materials	Therapies	loading capacities	Ref.
Dual-modal therapy	Zinc phthalocyanine loaded Pd@TiO_2	PDT, PTT	\	[1]
	Gd or radionuclide labeled fluorinated Pd nanosheets	PTT, RT	\	[2]
	Fe_3O_4-Pd Janus particles	magnetic-photo hyperthermia, CDT	\	[3]
	DOX@Pd Gel	Chemotherapy, PTT	\	[4]
	Pd-Cys@MTX@RGD	Chemotherapy, PTT	51% (MTX)	[5]
	HMSS-NH_2/DOX@Pd	CDT, PTT	9.2 (DOX)	[6]
	CD-PdNS/ZIF-8 Janus nanoparticles	Chemotherapy, PTT	20 (DOX)	[7]

Notes: list of abbreviations: PDT photodynamic therapy; PTT photothermal therapy; RT radiation therapy; CDT chemodynamic therapy.

Table S2. Pd loading amount in MIL-101-NH_2 sample determined by ICP-MS.

Sample	Pd (wt%)	Fe (wt%)
MIL-101-NH_2@Pd	1.6	16.2

Table S3. Comparison table of drug loading capacities of MOF-based drug delivery systems**.**

MOFs-based drug carriers	Drug	Loading capacities (wt%)	Ref.
MIL-100(Fe)	DOX•HCl	9	[8]
MIL-101(Fe)-NH_2	Camptothecine	3.9	[9]
MIL-100(Fe)	Azidothymidine tryphosphate (AZT-TP)	24	[10]
MIL-100(Fe)	Curcumin	33	[11]
MIL-100(Fe)	DOX•HCl	10	[12]
PEG-RGD-β-CDSS- MIL-101	DOX•HCl	13.4	[13]
CP5-capped UMCM-1-NH-Py	DOX•HCl	3.4	[14]
ZIF-8	DOX•HCl	20	[15]
ZIF-90	DOX•HCl	12.6	[16]
UiO-68	Cisplatin	12.3	[17]
Mi-UiO-68	DOX•HCl	4.84	[18]
DOX-MIL@Pd	DOX•HCl	47.3	This work

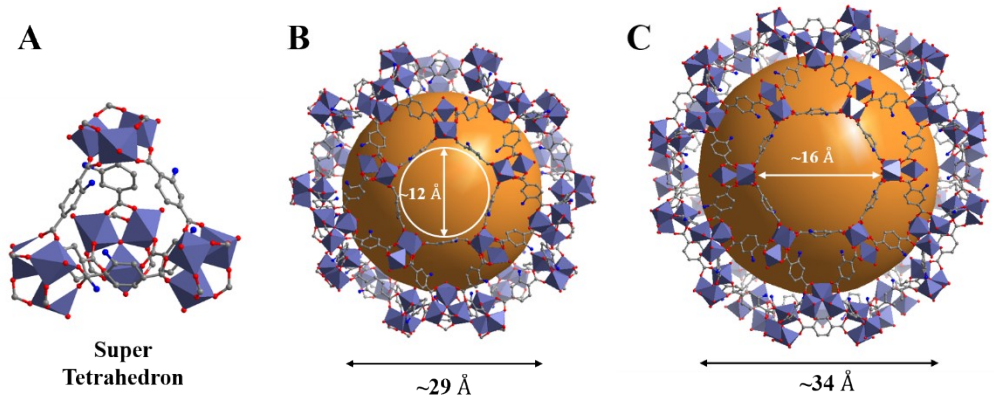

Figure S1. Structure of MIL-101(Fe)-NH_2. (A)the hybrid super tetrahedron formed by trimer of iron octahedral and the 2-aminoterephthalic acid; (B)(C) the two types of mesoporous cages (the cages highlighted with brown sphere and the Fe octahedron are shades in purple color).

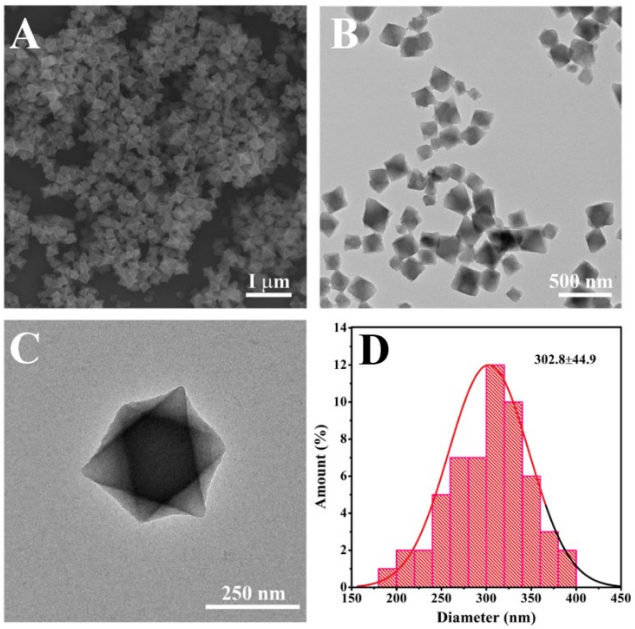

Figure S2. Morphology of MIL-101(Fe)-NH_2. (A) SEM image of MIL-101(Fe)-NH_2. (B) Large scale TEM image of MIL-101(Fe)-NH_2, and (C) TEM image of single MIL-101(Fe)-NH_2. (D) Corresponding size histogram of MIL-101(Fe)-NH_2 shown in (B).

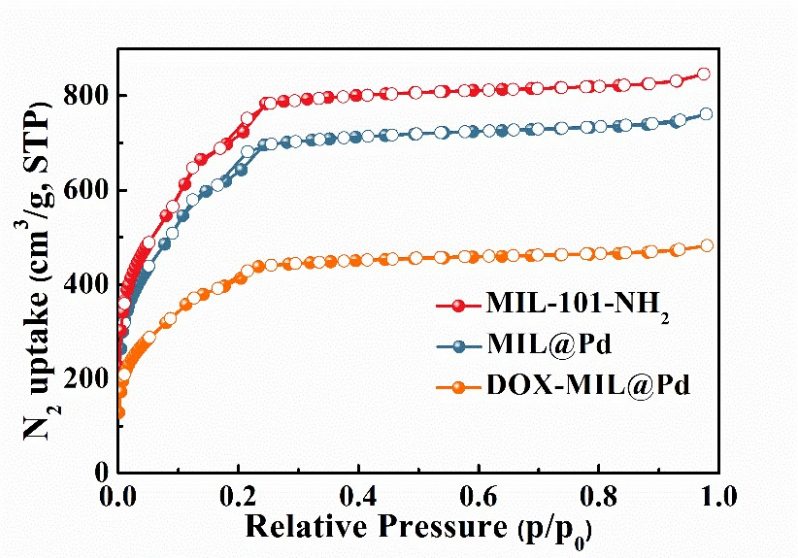

Figure S3. N_2 sorption isotherms for MIL-101-NH_2, MIL@Pd and DOX-MIL@Pd at 77 K. The corresponding surface areas are 2068, 1849, 1201 m^2/g, respectively.

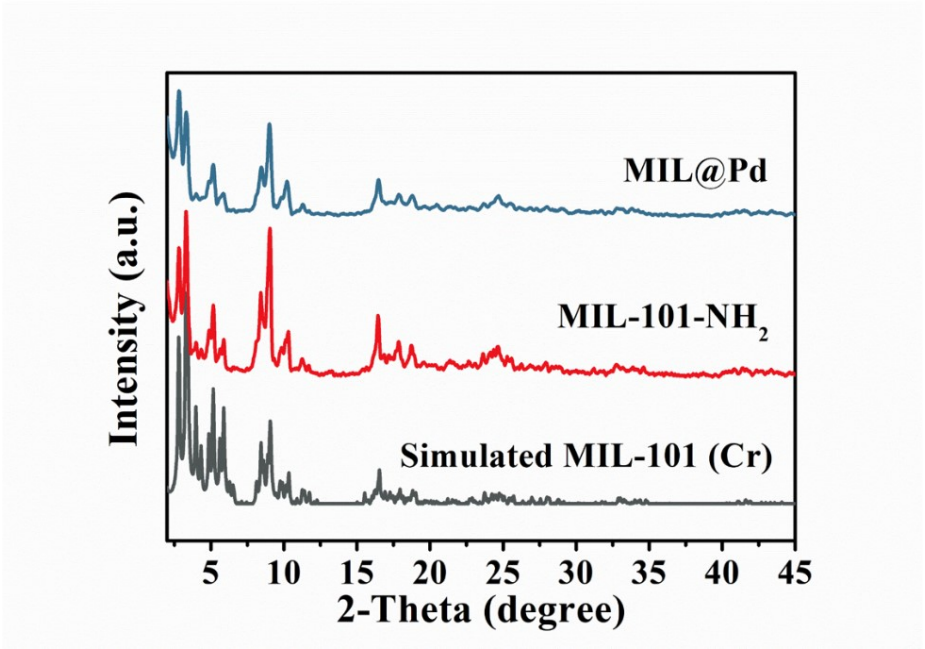

Figure S4. PXRD patterns of simulated MIL-101 (Cr), MIL-101-NH_2 and MIL@Pd NPs.

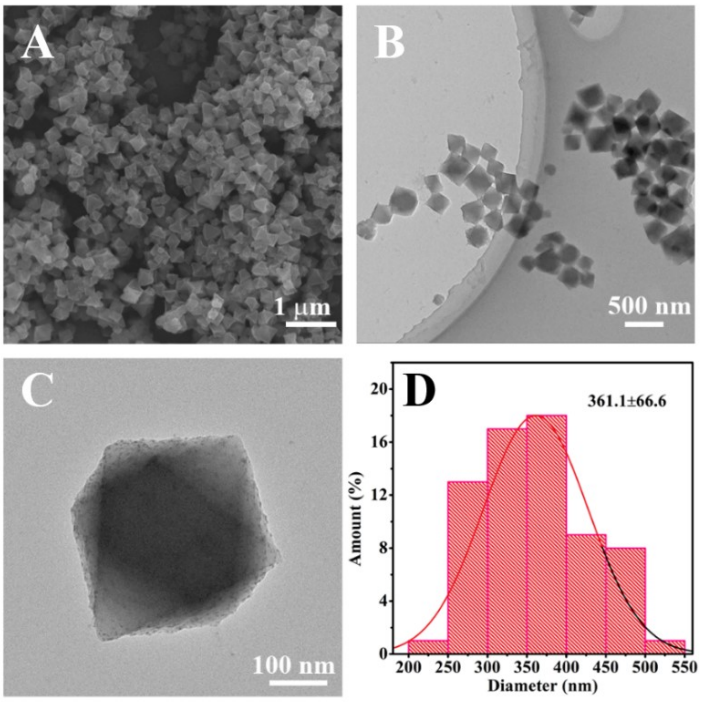

Figure S5. Morphology of MIL@Pd. (A) SEM image of MIL@Pd. (B) Large scale TEM image of MIL@Pd, and (C) TEM image of single MIL@Pd. (D) Corresponding size histogram of MIL@Pd shown in (B).

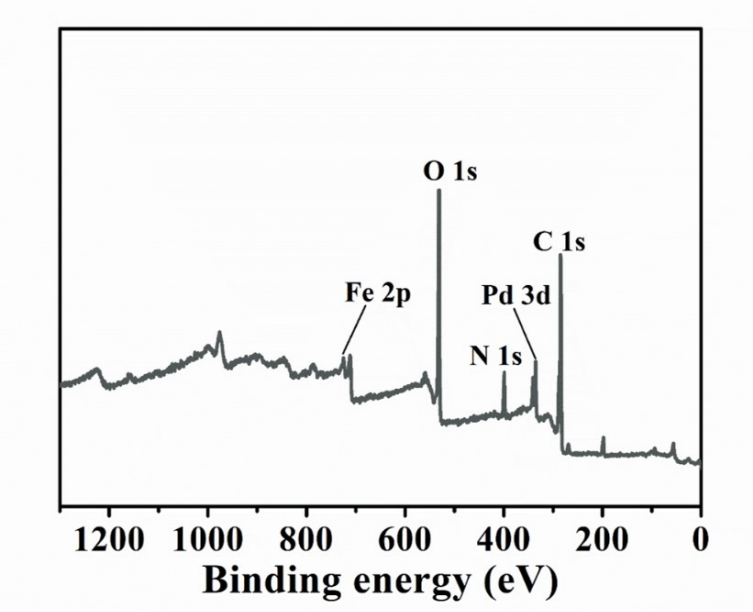

Figure S6. XPS spectra of MIL. Inserted tables are the atomic ratio of Fe and Pd elements.

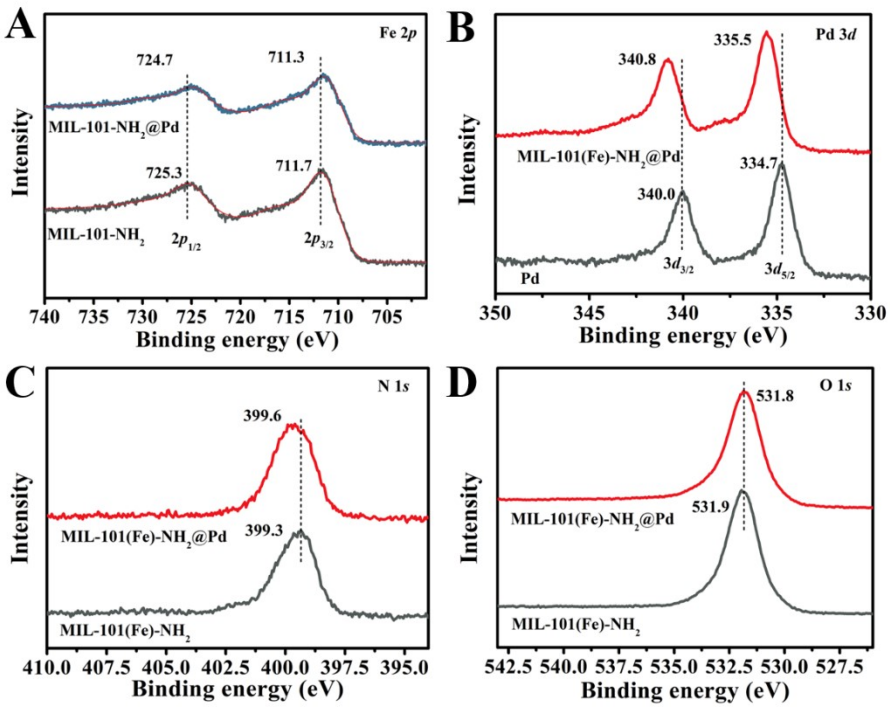

Figure S7. XPS profiles of Fe, Pd, N, O. (A) Fe 2*p* level. (B) Pd 3*d* level. (C) N 1*s* level. (D) 1*s* level.

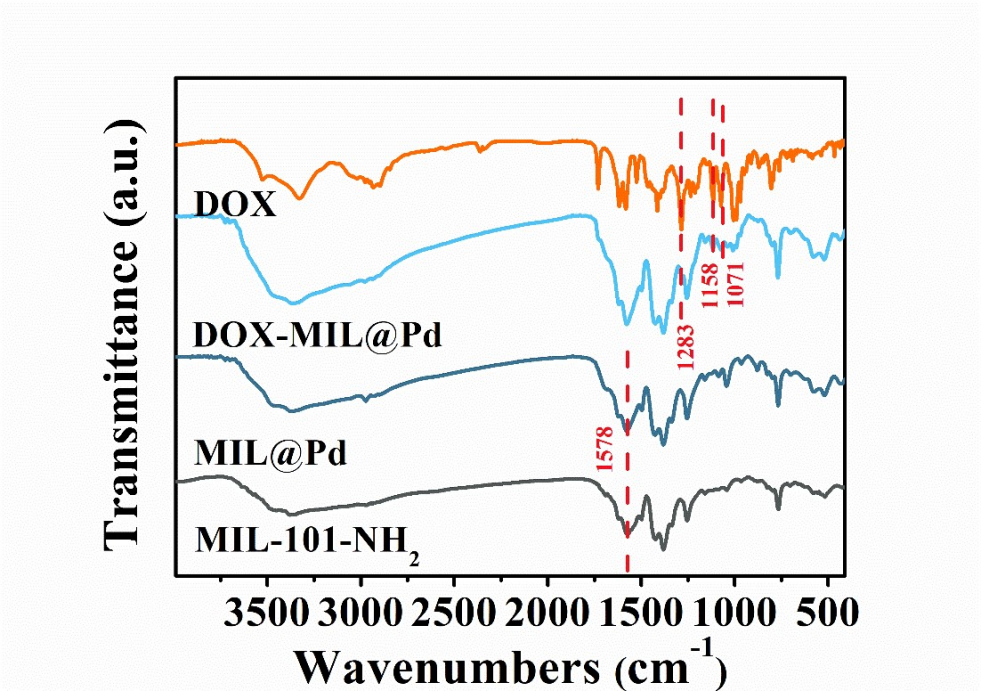

Figure S8. FTIR spectra of MIL-101-NH_2, MIL@Pd, DOX-MIL@Pd and DOX.

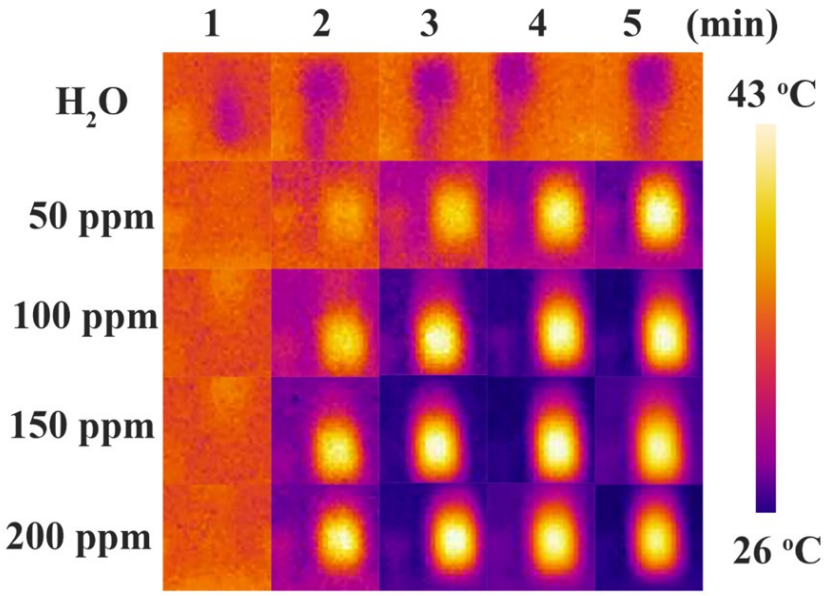

Figure S9. The infrared thermal images of water and MIL@Pd NPs with different concentration (50, 100, 150, 200 μg mL^{-1}) irradiated by 808 nm laser (at 2 W cm^{-2}) for 1-5 min.

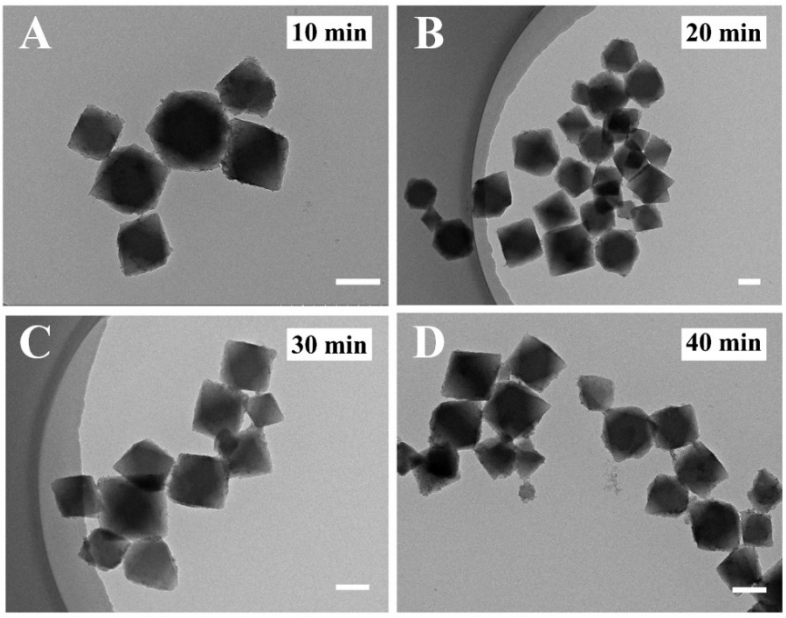

Figure S10. TEM images of MIL@Pd NPs irradiated by 808 nm laser (2 W cm^{-2}) for a series of time. Scale bar, 200 nm.

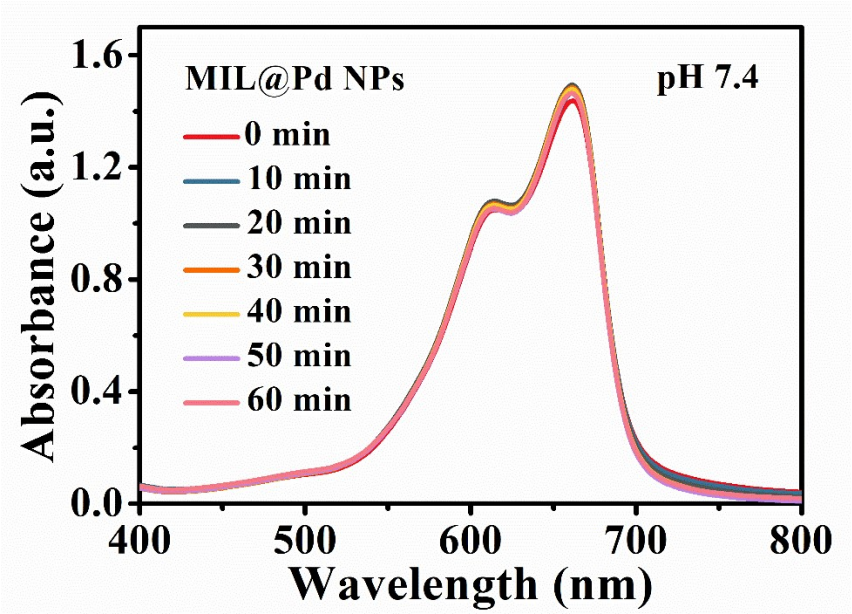

Figure S11. The change of absorbance as the function of reaction time at pH 7.4 under MIL@Pd catalysis.

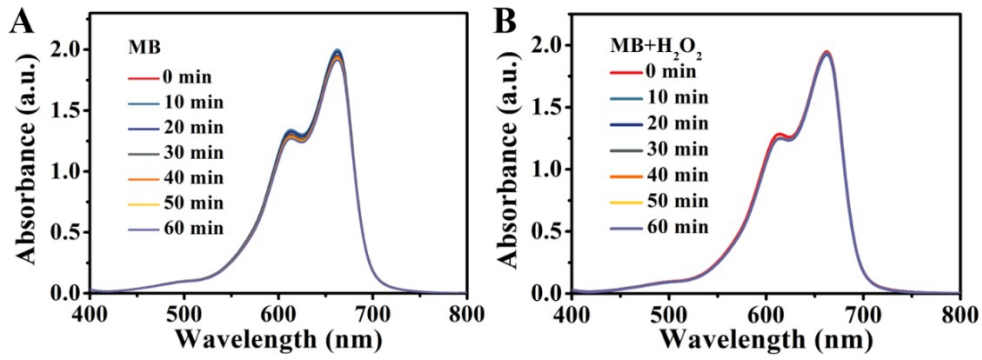

Figure S12. UV-vis spectra of MB (A) and treated with H_2O_2 (B).

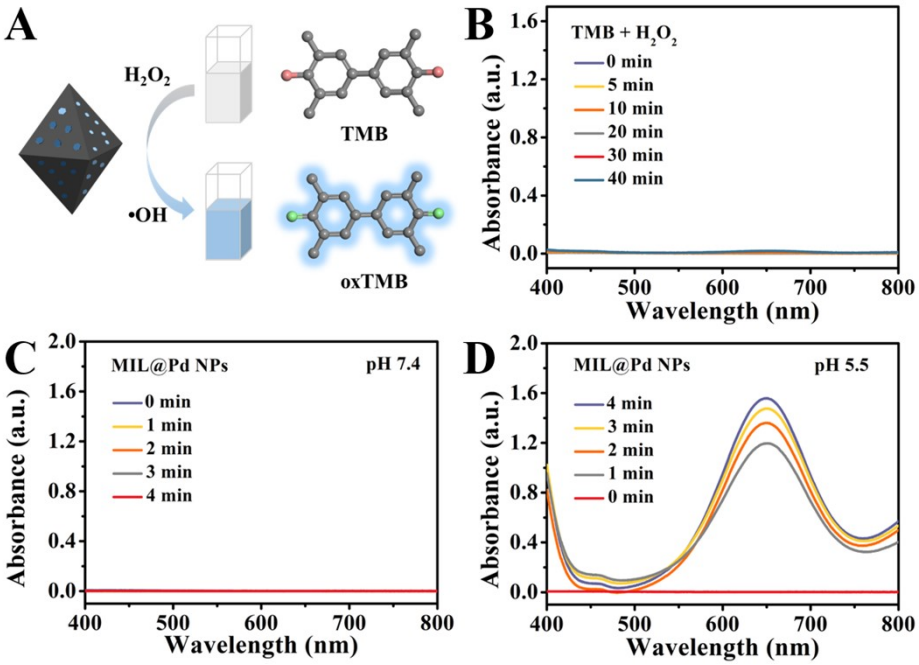

Figure S13. UV-vis spectra of TMB treated with H_2O_2 (B), MIL@Pd +H_2O_2 at pH 7.4 (C) or pH 5.5 (D).

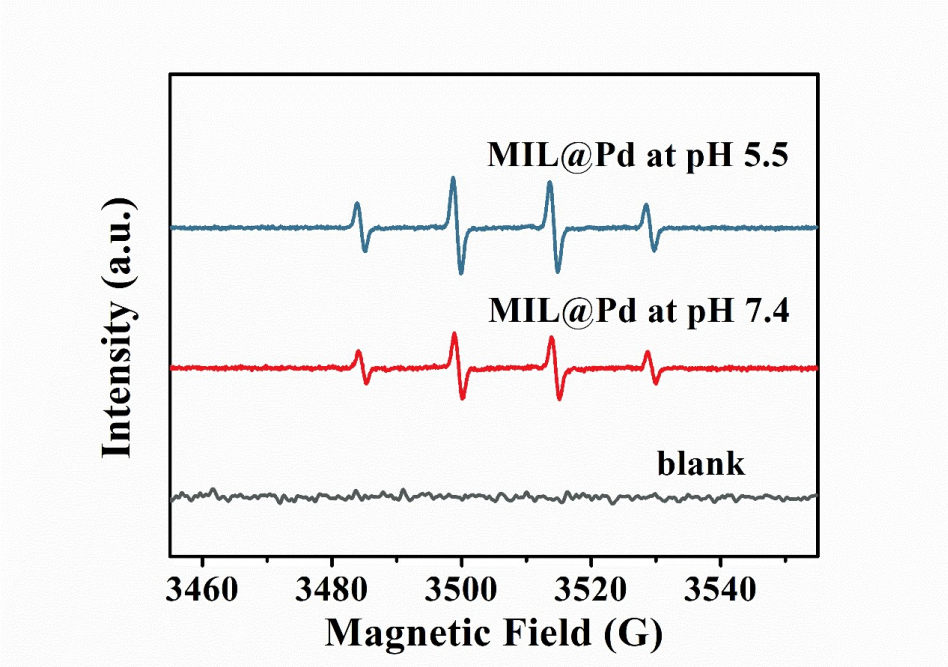

Figure S14. ESR spectra obtained with the addition of MIL@Pd at pH 7.4 and pH 5.5.

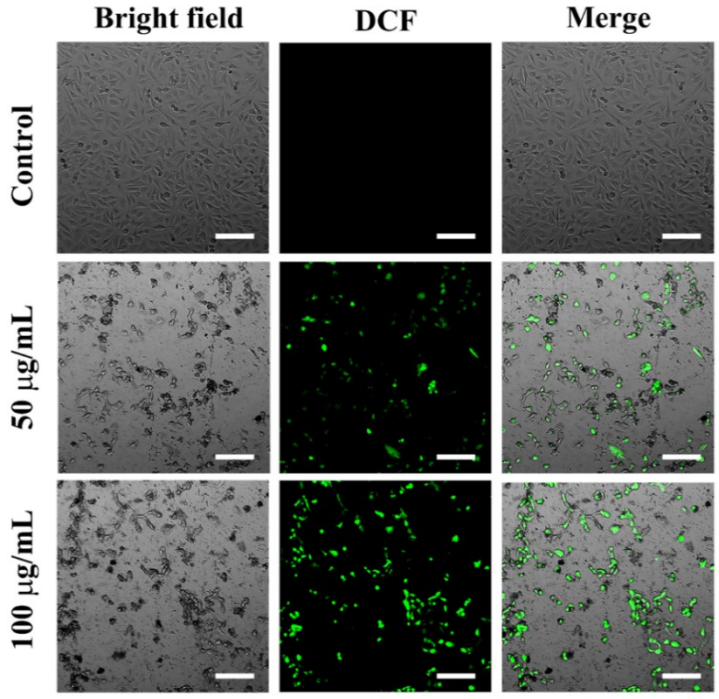

Figure S15. Intracellular ROS detection in Hela cells treated with MIL@Pd NPs with different concentration. Scale bar, 160 μm.

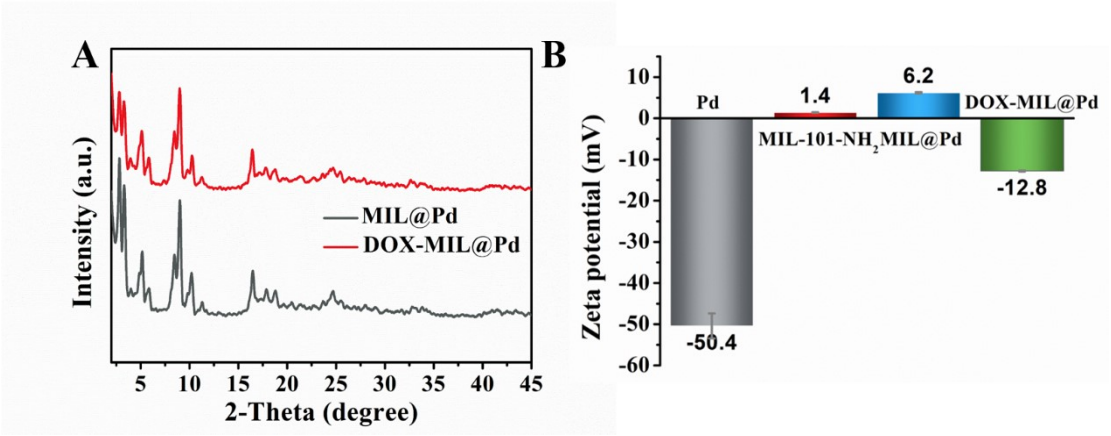

Figure S16. (A) PXRD patterns of MIL@Pd and DOX-MIL@Pd. (B) Zeta potential of Pd NSs, MIL-101-NH_2, MIL@Pd and DOX-MIL@Pd.

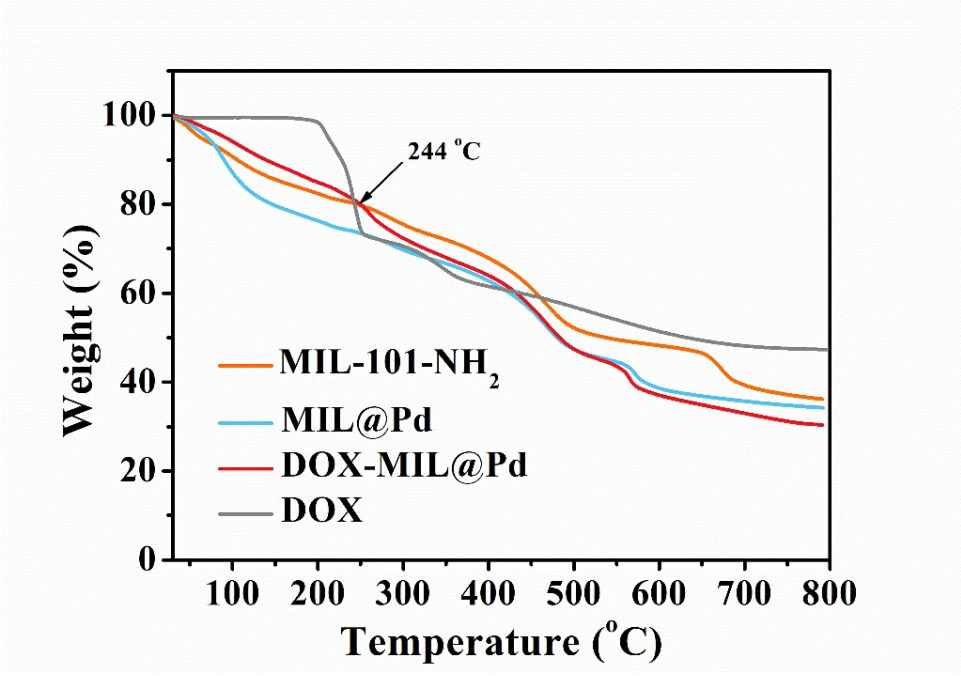

Figure S17. TGA curves of DOX, MIL-101-NH_2, MIL@Pd and DOX-MIL@Pd.

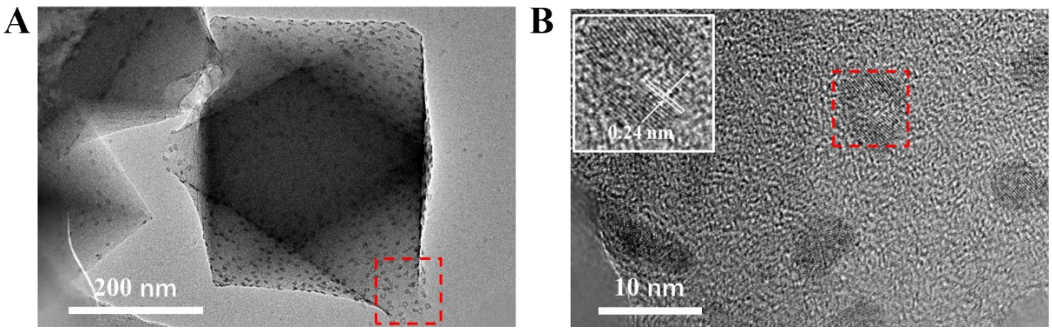

Figure S18. Characterization of Pd NSs on the DOX-MIL@Pd. (A) TEM images of DOX-MIL@Pd NPs. (B) The enlarged figure of dotted area in (A) and the lattice fringes (inset).

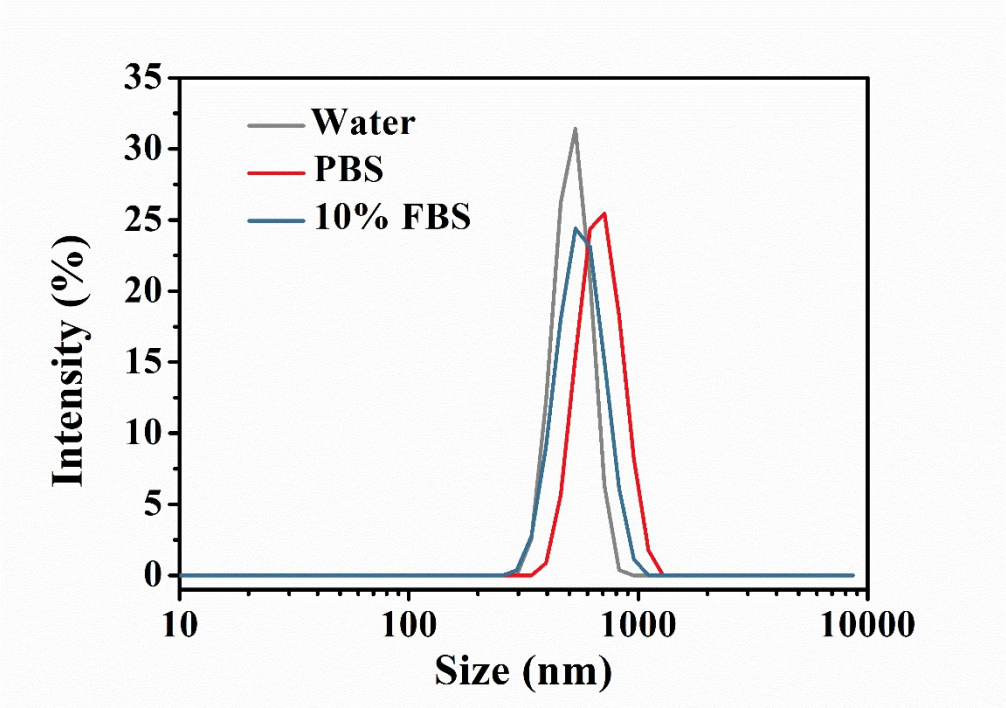

Figure S19. The DLS of DOX-MIL@Pd NPs in (a) water, (b) PBS, and (c) 10% FBS.

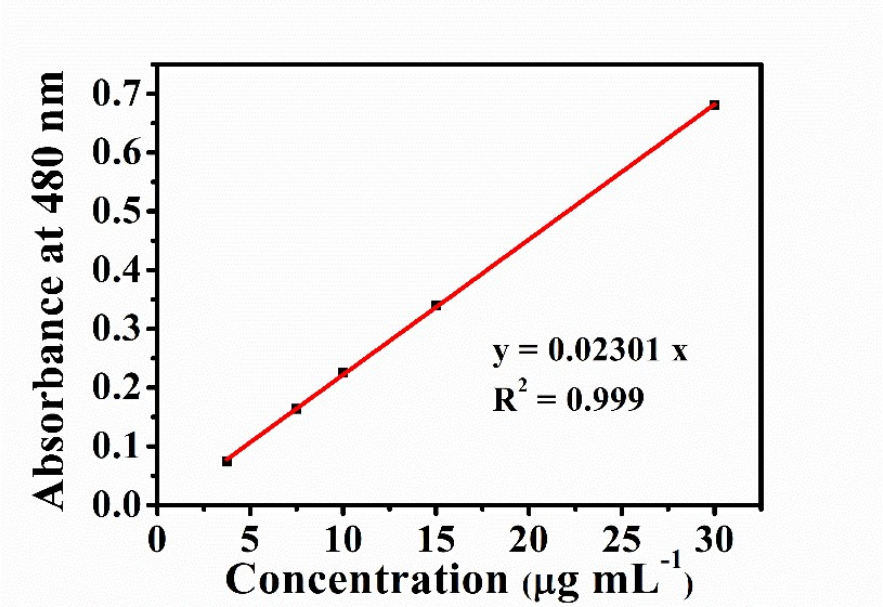

Figure S20. The relationship between the absorbance at 480 nm and the concentration of DOX solution.

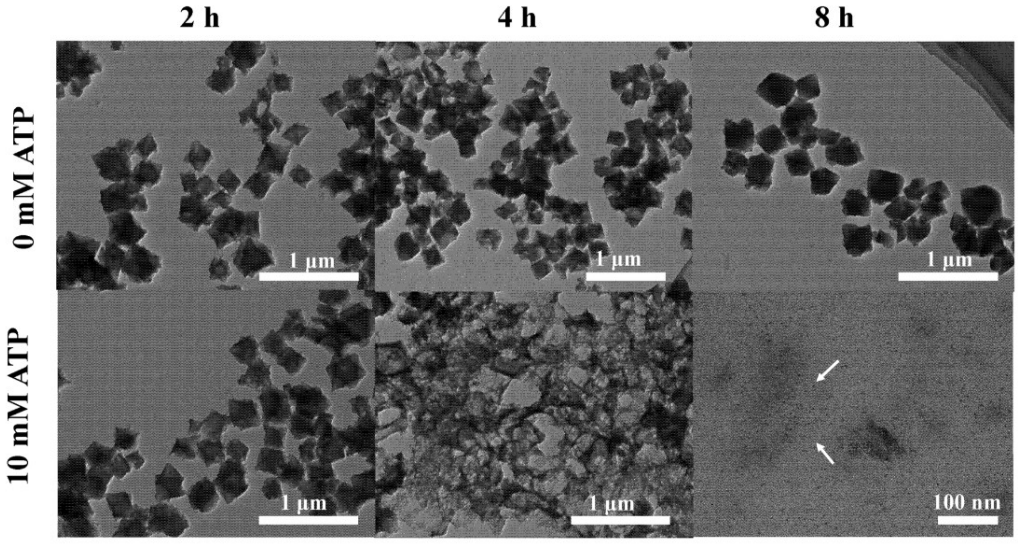

Figure S21. Degradation of DOX-MIL@Pd NPs at different time periods in the absence of ATP and in 10 mM ATP condition. White arrows reveal the remaining debris at the late stage of degradation.

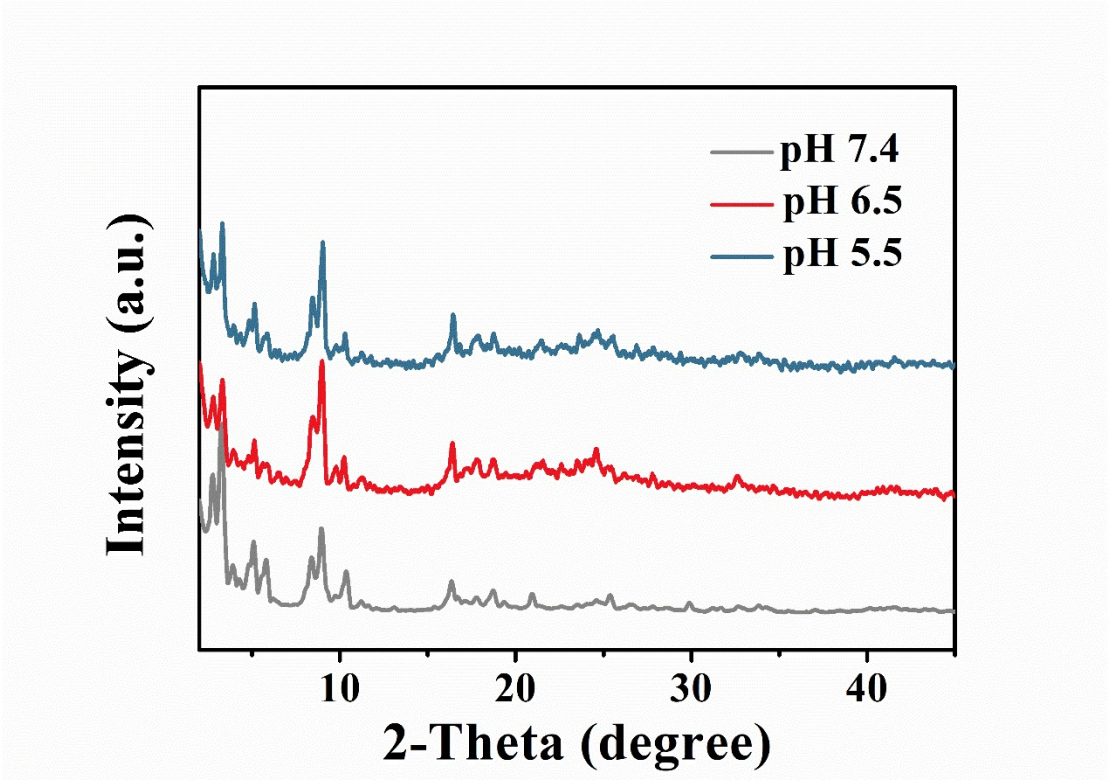

Figure S22. PXRD patterns of MIL-101-NH_2 treated with PBS buffer solutions at different pH for 2 days.

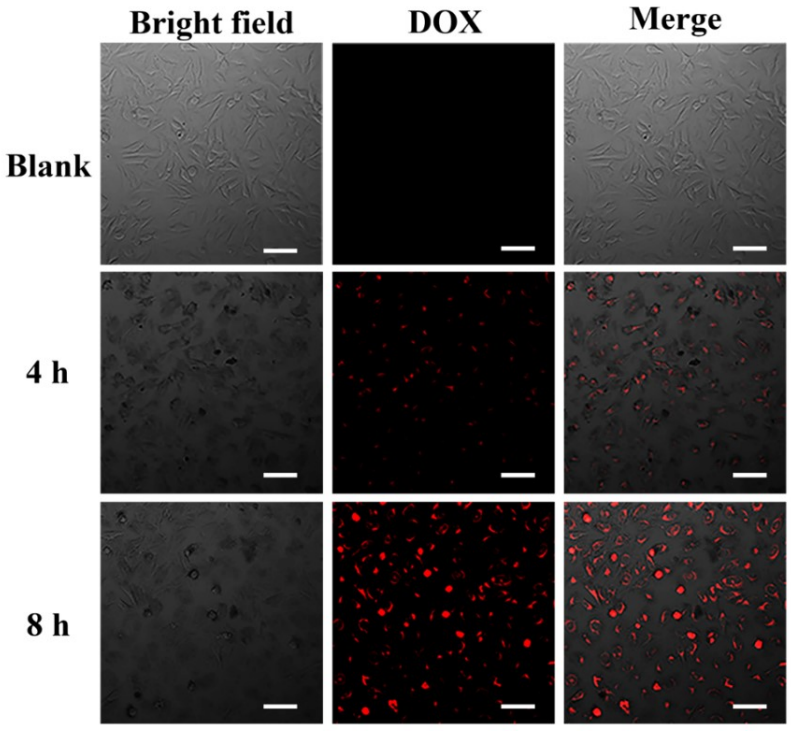

Figure S23. Confocal images of Hela cells treated with DOX-MIL@Pd after incubation for different time. Scale bar, 80 μm.

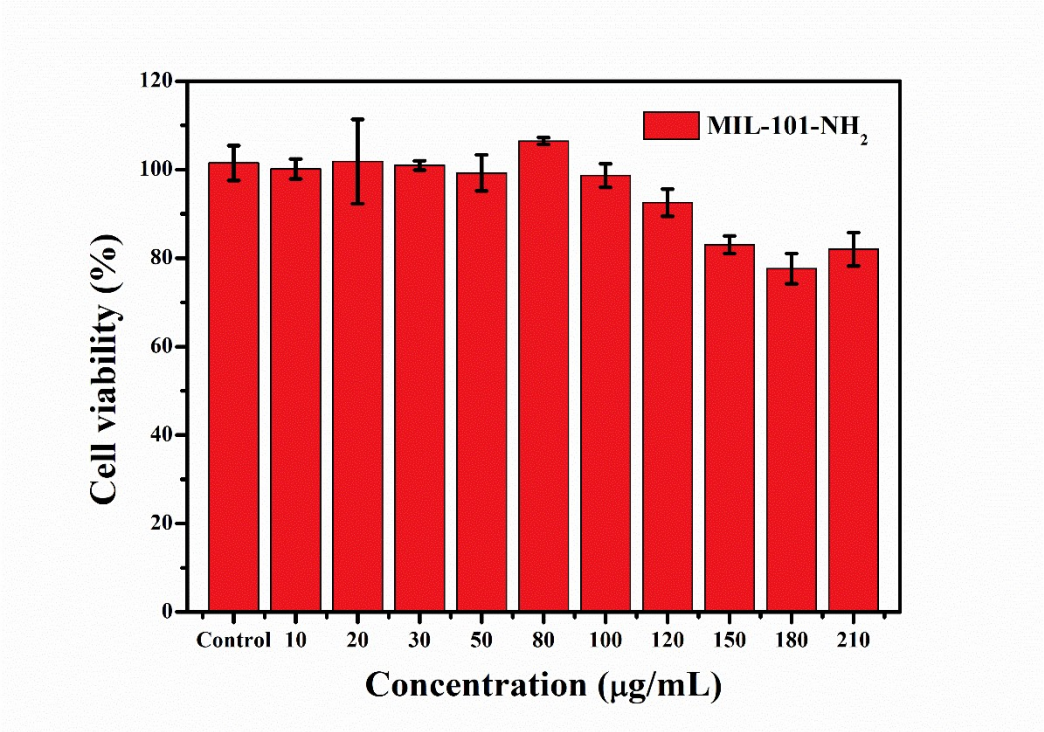

Figure S24. Hela cell viabilities of MIL-101-NH_2 NPs with different concentration.

References

1 C. Wang, Y. Li, W. Yang, L. Zhou and S. Wei, *Adv. Healthc. Mater*., 2021, **10**, 2100601.

2 Z. Guo, M. Chen, C. Peng, S. Mo, C. Shi, G. Fu, X. Wen, R. Zhuang, X. Su, T. Liu, N. Zheng and X. Zhang, *Biomaterials*, 2018, **179**, 134-143.

3 X. Ma, Y. Wang, X. Liu, H. Ma, G. Li, Y. Li, F. Gao, M. Peng, H.M. Fan and X. Liang, *Nanoscale Horiz*., 2019, **4**, 1450-1459.

4 Y.W. Jiang, G. Gao, P. Hu, J.B. Liu, Y. Guo, X. Zhang, X.W. Yu, F.G. Wu and X. Lu, *Nanoscale*, 2020, **12**, 210-219.

5 X. Chen, X. Zhu, T. Xu, M. Xu, Y. Wen, Y. Liu, J. Liu and X. Qin, *J. Mat. Chem. B*, 2019, **7**, 112-122.

6 W. Fang, S. Tang, P. Liu, X. Fang, J. Gong and N. Zheng, *Small*, 2012, **8**, 3816-3822.

7 L. Zhang, S. Li, X. Chen, T. Wang, L. Li, Z. Su and C. Wang, *Adv. Funct. Mater*., 2018, **28**, 1803815.

8 P. Horcajada, T. Chalati, C. Serre, B. Gillet, C. Sebrie, T. Baati, J. F. Eubank, D. Heurtaux, P. Clayette, C. Kreuz, J. Chang, Y. K. Hwang, V. Marsaud, P. Bories, L. Cynober, S. Gil, G. Férey, P. Couvreur and R. Gref, *Nat. Mater*., 2010, **9**, 172-178.

9 J. Liu, L. Zhang, J. Lei, H. Shen and H. Ju, *ACS Appl. Mater. Interfaces*, 2017, **9**, 2150-2158.

10 V. Agostoni, T. Chalati, P. Horcajada, H. Willaime, R. Anand, N. Semiramoth, T. Baati, S. Hall, G. Maurin, H. Chacun, K. Bouchemal, C. Martineau, F. Taulelle, P. Couvreur, C. Rogez-Kreuz, P. Clayette, S. Monti, C. Serre and R. Gref, *Adv. Healthc. Mater*., 2013, **2**, 1630-1637.

11 Y. Zhang, L. Wang, L. Liu, L. Lin, F. Liu, Z. Xie, H. Tian and X. Chen, *ACS Appl. Mater. Interfaces*, 2018, **10**, 41035-41045.

12 Z. Dong, Y. Sun, J. Chu, X. Zhang and H. Deng, *J. Am. Chem. Soc*., 2017, **139**, 14209-14216.

13 X. Wang, Z. Dong, H. Cheng, S. Wan, W. Chen, M. Zou, J. Huo, H. Deng and X. Zhang, *Nanoscale*, 2015, **7**, 16061-16070.

14 L. L. Tan, H. Li, Y. C. Qiu, D. X. Chen, X. Wang, R. Y. Pan, Y. Wang, S. X. Zhang, B. Wang and Y. W. Yang, *Chem. Sci*., 2015, **6**, 1640-1644.

15 H. Zheng, Y. Zhang, L. Liu, W. Wan, P. Guo, A. M. Nyström and X. Zou, *J. Am. Chem. Soc*., 2016, **138**, 962-968.

16 Z. Jiang, Y. Wang, L. Sun, B. Yuan, Y. Tian, L. Xiang, Y. Li, Y. Li, J. Li and A. Wu, *Biomaterials*, 2019, **197**, 41-50.

17 C. He, K. Lu, D. Liu and W. Lin, *J. Am. Chem. Soc.*, 2014, **136**, 5181-5184.